The role of oxygen incorporation in Ni (111) substrates on the growth of hexagonal boron nitride monolayers

IOP Publishing Nanotechnology
Nanotechnology 34 (2023) 505602 (14pp) https://doi.org/10.1088/1361-6528/acfaa8

The role of oxygen incorporation in Ni (111) substrates on the growth of hexagonal boron nitride monolayers

Yuan Li[1], Hector Gomez[1], Jason Tran[2], Yanwei He[1], Chengyun Shou[1], Tianchen Yang[1], Peng Wei[2], Roger K Lake[1] and Jianlin Liu[1,*]

[1] Department of Electrical and Computer Engineering, University of California, Riverside, CA 92521, United States of America
[2] Department of Physics and Astronomy, University of California, Riverside, CA 92521, United States of America

E-mail: jianlin@ece.ucr.edu

Received 13 July 2023, revised 7 September 2023
Accepted for publication 17 September 2023
Published 5 October 2023

Abstract

Reliable and controllable growth of two-dimensional (2D) hexagonal boron nitride (h-BN) is essential for its wide range of applications. Substrate engineering is one of the critical factors that influence the growth of the epitaxial h-BN films. Here, we report the growth of monolayer h-BN on Ni (111) substrates incorporated with oxygen atoms via molecular beam epitaxy. It was found that the increase of incorporated oxygen concentration in the Ni substrate through a pretreatment process prior to the h-BN growth step would have an adverse effect on the morphology and growth rate of 2D h-BN. Under the same growth condition, h-BN monolayer coverage decreases exponentially as the amount of oxygen incorporated into Ni (111) increases. Density functional theory calculations and climbing image nudged elastic band (CI-NEB) method reveal that the substitutional oxygen atoms can increase the diffusion energy barrier of B and N atoms on Ni (111) thereby inhibiting the growth of h-BN films. As-grown large-area h-BN monolayer films and fabricated Al/h-BN/Ni (MIM) nanodevices were comprehensively characterized to evaluate the structural, optical and electrical properties of high-quality monolayers. Direct tunneling mechanism and high breakdown strength of $\sim$11.2 MV cm^{-1} are demonstrated for the h-BN monolayers grown on oxygen-incorporated Ni (111) substrates, indicating that these films have high quality. This study provides a unique example that heterogeneous catalysis principles can be applied to the epitaxy of 2D crystals in solid state field. Similar strategies can be used to grow other 2D crystalline materials, and are expected to facilitate the development of next generation devices based on 2D crystals.

Supplementary material for this article is available online

Keywords: two dimensional (2D) materials, hexagonal boron nitride (h-BN), molecular beam epitaxy (MBE), catalyst-assisted growth

(Some figures may appear in colour only in the online journal)

1. Introduction

Atomically thin hexagonal boron nitride (h-BN) has drawn tremendous attention for next-generation electronics owing to its excellent properties, wide bandgap ($\sim$5.9 eV) [1], high electric breakdown strength ($\sim$12 MV cm^{-1}), high thermal conductivity ($\sim$600 Wm^{-1}K^{-1}), excellent thermal/chemical stability, and a surface free of dangling bonds [2–4]. Due to these remarkable properties, h-BN has been adopted perfectly as an insulating layer in capacitors [5, 6], transistors [7–11],

* Author to whom any correspondence should be addressed.

an active layer for resistive switching memristors [12–16], single-photon emitters [17–19], and ultra-flat anti-scattering substrate and encapsulation layer [20–24] for van der Waals materials nanodevices. All of these applications propose strict requirements on h-BN quality and demand for large-scale reliable and controllable synthesis methodologies to achieve high quality 2D h-BN films [25].

The exfoliation method is the most used method to obtain high-quality 2D flakes for research purposes since the discovery of exfoliated graphene in 2004 [26]. Even though many exfoliation techniques have been developed during the last decades [27–30], exfoliated flakes are normally very small with non-uniform sizes and thicknesses, so that exfoliation is not a scalable method to produce h-BN films. The bottom-up synthesis of h-BN films such as chemical vapor deposition (CVD) and physical vapor deposition (PVD) provides larger size continuous h-BN films. However, one of the unresolved problems is that epitaxial h-BN films often possess higher defect densities than those obtained through high-temperature high-pressure methods, such as adventitious impurities [31], grain boundaries [32, 33], and nucleation point [34, 35], which result in scattering or pinning of charge carriers between adjacent conducting layers that impair device performance.

One of the methods to reduce the defect density and achieve higher quality is to grow single-crystal h-BN film. Lee *et al* achieved the growth of wafer-scale single-crystal h-BN films by means of self-collimation of B and N edges induced by electrostatic interaction between grains to eventually form a single-crystalline monolayer on a melted Au substrate [36]. Wang *et al* reported epitaxial growth of a 100 square-centimeter single-crystal h-BN monolayer on a low-symmetry Cu (110) surface with the aid of Cu <211> step edges coupling with h-BN zigzag edges to enable large domain unidirectional alignment [2]. Chen *et al* reported top-edge Cu step edges assisted growth of h-BN monolayer on single-crystal annealed high-symmetry Cu (111) surface [37]. Cheng *et al* demonstrated the plasma-assisted MBE growth of mono- and few-layer h-BN on highly orientated pyrolytic graphite (HOPG) substrates at high temperatures $\sim$ 1390 °C [38]. Our previous effort also led to the synthesis of a large-area single-crystal h-BN monolayer on an annealed single-crystal Ni (111) substrate [5]. However, these successful growths of h-BN relied on the preparation of perfect high-purity single-crystal metal substrates, which are rather complicated and expensive. A cost-effective way is to carry out a secondary recrystallization process on polycrystalline transition metal substrates to form very large single-crystal grains in the substrate for 2D h-BN growth [39]. Another strategy for achieving wafer-scale 2D h-BN single crystal growth is the enhancement of the catalytic strength of the transition metal substrate. Our group reported that the incorporation of carbon in Co and Ni substrates as interstitial can improve the adsorption of B and N atoms and reduce the diffusion barrier, resulting in wafer-scale 2D h-BN films with uniform thickness [4, 39–42]. The embedded carbon interstitial has effectively influenced the d-orbital electronic structures of the transition metal, leading to the enhanced catalytic effect. Similar substrate engineering approaches achieved by other groups include nucleation control and growth speed control for large domain h-BN monolayers by Si-doped Fe substrates [43], iron boride (Fe_2B) alloy [44], and Fe–Cr flux [45]. Also, oxygen-assisted chemical vapor deposition growth of 2D h-BN on copper foils was demonstrated to suppress nucleation density and enhance the size of 2D h-BN domains [46, 47]. It should be noted that the incorporation of different impurities in transition metal substrates does not always lead to enhanced catalyst strength of the substrates and increased growth speed of 2D crystals, for example, the growth speed of h-BN monolayer is significantly reduced on carburized single-crystal Ni(111) substrates [3]. Previous efforts on the role of modification in transition metal substrates on the growth speed of 2D h-BN layers compared with direct growth on pristine substrates are summarized in table S1 in the supporting materials. Although oxygen incorporation in copper can enhance the growth of 2D h-BN [46, 47], the role of oxygen incorporation in nickel substrates on 2D h-BN growth was not studied and the underlying growth mechanism remains unknown.

In this work, we studied the role of the incorporation of oxygen atoms in Ni (111) substrates on the growth of h-BN monolayers both experimentally and theoretically. Ni (111) substrates were obtained by high temperature thermal annealing Ni foils at 1400 °C. After that, pre-annealed Ni foils were further electropolished to achieve fresh and flat surfaces. Monolayer h-BN films with different growth conditions were grown by MBE. Scanning electron microscopy (SEM) was used to characterize the morphology and coverage of the h-BN films. Surface and depth-profiling x-ray photoelectron spectroscopy (XPS) was used to characterize the sample surface elements bonding and concentrations. Coverage-dependent reflection high-energy electron diffraction (RHEED) was employed to analyze the epitaxial relationship between h-BN film and substrates. Density function theory (DFT) and climbing image nudged elastic band (CI-NEB) methods were employed to explain the experimental results. Metal/h-BN/metal (MIM) devices based on monolayer h-BN film were fabricated to study the nano-capacitance, and electrical breakdown.

2. Experimental methods

2.1. h-BN growth

Nickel (Ni) foils with a thickness of 0.1 mm and a purity of 99.995% from Alfa Aesar were first annealed at a high temperature of 1400 °C to obtain single crystal Ni (111) foils. Then annealed foils were electropolished and cut into 1 cm x 1 cm pieces as substrates. Electropolishing took place in the electrolyte mixed with DI water, sulfuric acid (H_2SO_4, 96%), and phosphorous acid (H_3PO_3, 85%) in the ratio of 3:4:7. The polished substrate was rinsed in DI water to remove chemical residue. These substrates were degreased and deoxidized in isopropyl alcohol (IPA, C_3H_8O) solution, diluted hydrochloric acid (HCl) (10%), rinsed in deionized (DI) water,

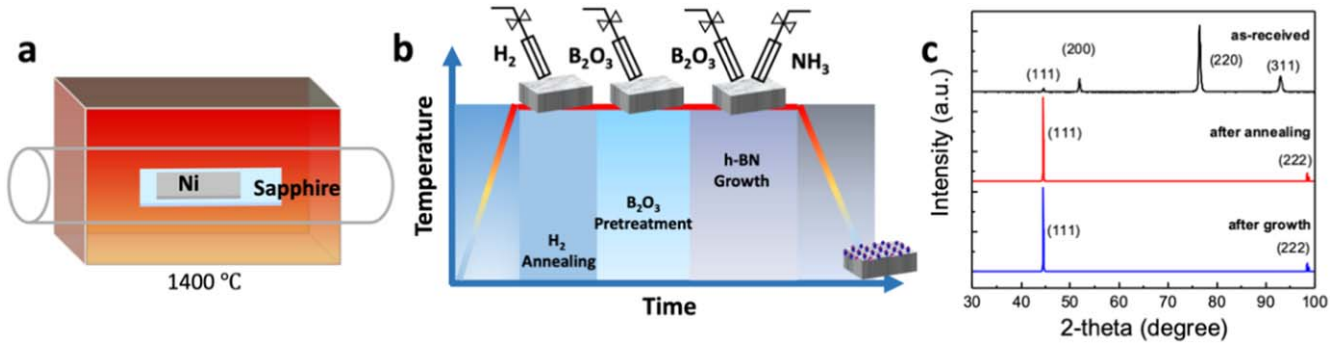

Figure 1. (a) Schematic of high temperature annealing of Ni (111) substrates for h-BN growth. (b) Schematic of h-BN monolayer growth procedure including sequential hydrogen annealing, oxygen incorporation and h-BN growth. (c) XRD pattern in a $\theta - 2\theta$ scan mode of as received Ni foil, the same foil after thermal annealing and after h-BN growth.

nitrogen gun blown dry, and finally loaded into a Perkin–Elmer MBE system with a background pressure of 10^{-9} Torr. A Knudsen effusion cell filled with boron oxide powder (B_2O_3, Alfa Aesar, 99.999% purity) was used as boron source. High purity ammonia (NH_3, American Gas Group, 99.9995% purity) were used as nitrogen source through a mass flow controller. All samples were grown at 870 °C with 10 sccm ammonia (NH_3) and boron oxide (B_2O_3) effusion cell at 1170 °C.

2.2. Film characterization

SEM images were acquired using a TESCAN Vega 3 scanning electron microscopy in secondary electron (SE) imaging mode. XPS spectra were acquired using a Kratos AXIS ULTRA XPS system equipped with an Al K-Alpha x-ray source (photon energy of 1486.7 eV) and a 165 mm mean radius electron energy hemispherical analyzer. The vacuum pressure was kept below 3×10^{-9} Torr during the acquisition. The photoelectrons have a take-off angle of 90° to the surface, where detected electrons originate from the sample surface with a trajectory in line with the surface normal. XRD spectra were acquired using a Panalytical Empyrean Series 2 system equipped with a Cu K-Alpha x-ray source. UV–vis absorption spectra were obtained using an Agilent Cary 5000 double beam UV–vis spectrophotometer. Raman spectra were obtained using a confocal HORIBA LabRam microscope equipped with a 60 mW 532 nm laser. AFM images were acquired using tapping mode of a Veeco D5000 AFM system. STM images were acquired using Nanosurf Naio STM system. HRTEM images and SAED pattern were acquired using ThermoFisher Scientific Titan Themis 300 system.

2.3. Theoretical calculations

First-principles density functional theory (DFT), utilizing the Vienna *Ab Initio* Package (VASP), was implemented to calculate the adsorption and diffusion energies of the Ni(111) surfaces. All calculations used the Perdew–Burke–Ernzenhof (PBE) variation of the generalized gradient approximation (GGA) and the projector-augmented wave (PAW) method. A converged plane-wave energy cut-off of 600 eV and a k-point mesh of $4 \times 4 \times 1$ is used for relative accuracy with reduced computational cost. The pristine surface consists of a $4 \times 4 \times 4$ slab with 64 nickel (Ni) atoms. Similarly, the oxygen-incorporated surfaces consist of one and two Ni atoms replaced with oxygen (O) atoms to simulate the more stable substitutional point defects. The adsorption energies are calculated using a single B or N atom along the path between an HCP site and an adjacent HCP site. The climbing image nudged elastic band method (CI-NEB) was implemented to elucidate the barrier height associated with diffusing B or N atoms between adsorption sites.

2.4. Device fabrication and characterization

Metal–insulator–metal devices were fabricated by depositing 100 nm Al metal contact onto as-grown h-BN on Ni (111) substrate sample by a standard photolithography and lift-off process using Karl Suss Model MA-6 mask aligner system and Temescal BJD E-Beam evaporator system. *I–V* measurements were carried out by an Agilent 4155 C semiconductor parameter analyzer. *C–V* measurements were carried out by an Agilent 4284 A precision LCR meter.

3. Results and discussion

3.1. Growth and characterization of h-BN monolayers on oxygen incorporated Ni (111)

Figure 1(a) shows a schematic of the thermal annealing process of Ni foils in a ceramic tube high-temperature furnace using c-sapphire (Al_2O_3) as sample holder at 1400 °C for 90 min. A mixture of 200 sccm Ar and 200 sccm H_2 gases was used as protection gas flowing through the tube during the annealing and the tube pressure was controlled at 500 Torr.

Figure 1(b) shows a schematic of the h-BN monolayer growth procedure with boron oxide (B_2O_3) pretreatment. The growth conditions and parameters are shown in table S2 in the supporting information. The substrate was first heated to 870 °C and annealed at this temperature in 10 sccm hydrogen (H_2) condition for 15 min to remove any possible adventitious contaminations at the substrate surface. Then, the shutter of the B_2O_3 effusion cell at 1170 °C was opened, the Ni (111)

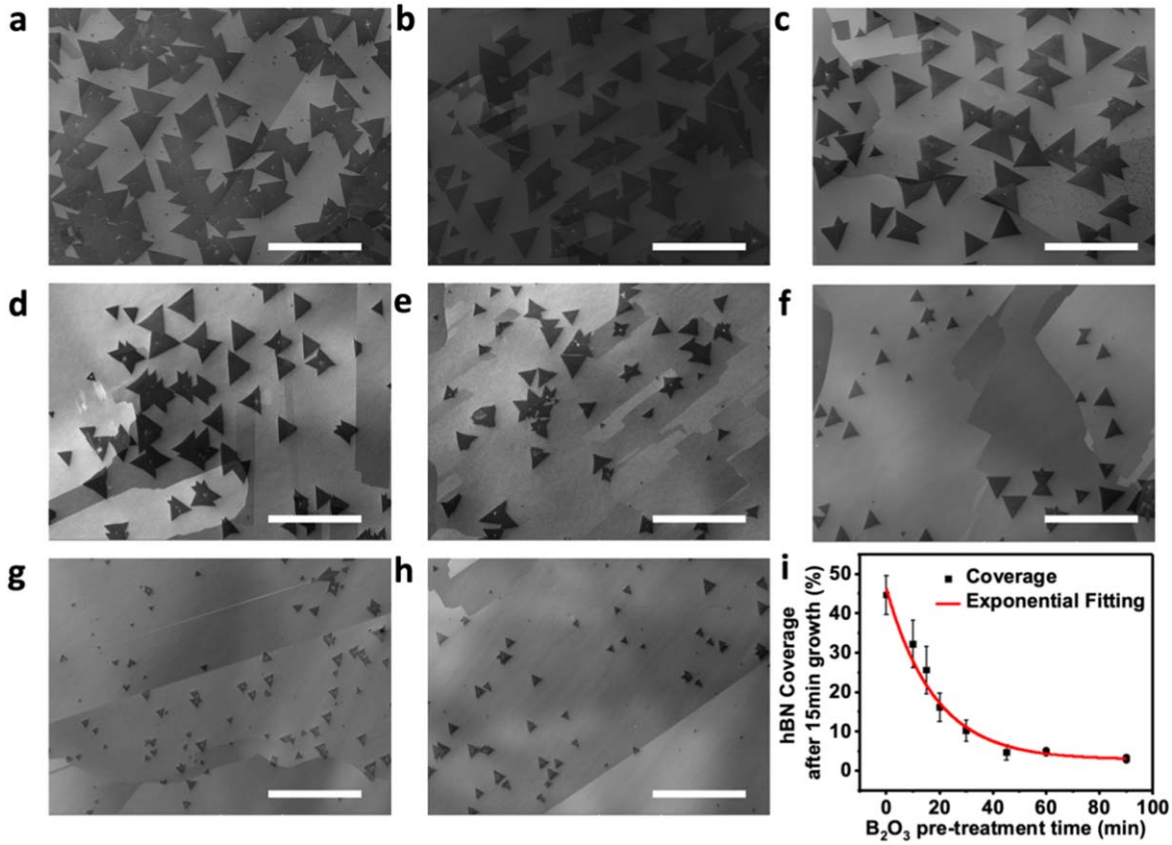

Figure 2. (a)–(h) SEM images of h-BN monolayer samples on Ni (111) substrates with different B_2O_3 pretreatment time, 0, 10, 15, 20, 30, 45, 60, and 90 min, respectively, then followed by fixed 15 min h-BN growth. All scale bars here are 500 μm. (i) The coverage of h-BN, exhibiting an exponential decay relationship with the increase of pretreatment time.

substrates were treated with B_2O_3 from 0 to 90 min for different samples. The purpose of this step is to incorporate oxygen atoms into the substrate with different concentrations to tune the catalytic strength of the substrate while B atoms have negligible incorporation as shown in the x-ray photoelectron spectroscopy (XPS) results later. It is noted that while direct oxidation of hot Ni substrates by leaking a small amount of oxygen gas into the MBE chamber may be a more straightforward way to incorporate oxygen atoms into the substrates, our B_2O_3 treatment to introduce oxygen into Ni substrate is a convenient and feasible approach since our MBE system has the B_2O_3 effusion cell but no oxygen gas line. After B_2O_3 pretreatment, both B and N sources were introduced into the chamber at the same time to start the epitaxial growth of h-BN at 870 °C with 10 sccm ammonia (NH_3) and B_2O_3 effusion cell at 1170 °C. By controlling the growth time, the morphology of h-BN monolayer samples evolves from small flakes to larger domains, to continuous films.

Figure 1(c) presents the x-ray diffraction (XRD) characterization results of as received and annealed Ni substrates, and a sample after h-BN growth. As seen from figure 1(c), XRD patterns show the evolution from pristine Ni substrate with different crystallographic orientations to annealed Ni substrate with only one dominant (111) orientation. In addition, the sample with h-BN on top exhibits Ni (111) surface orientation only, indicating that the growth of h-BN did not change the substrate orientation property.

Figure 2 shows SEM characterization results of h-BN coverage for the samples with different duration of B_2O_3 pretreatment of Ni (111) substrates. All samples were grown at the same condition at 870 °C with 10 sccm NH_3 and B_2O_3 effusion cell at 1170 °C for 15 min, except with different B_2O_3 pretreatment time, from 0, 10, 15, 20, 30, 45, 60, to 90 min, respectively. Figures 2(a)–(h) show SEM images of the samples, showing the morphology evolution of h-BN monolayers. As seen from the images, flake sizes and nucleation densities decrease with the increase of B_2O_3 pretreatment time. Then, the area coverages of the h-BN monolayers on the substrates were obtained by ImageJ software. Specifically, the coverages are 44.63%, 32.17%, 25.61%, 16.13%, 10.17%, 4.64%, 4.81%, and 2.96% for the samples on Ni (111) substrates with 0, 10, 15, 20, 30, 45, 60, 90 min B_2O_3 pretreatment time, respectively. Figure 2(i) shows a plot of the h-BN monolayer coverage as a function of B_2O_3 pretreatment time. The fitted curve exhibits an exponential decay relationship between the coverage and the pretreatment time t. The exponential decay function can be expressed as

$$A_{BN} = A_0 \exp\left(-\frac{t}{t_0}\right) + B \tag{1}$$

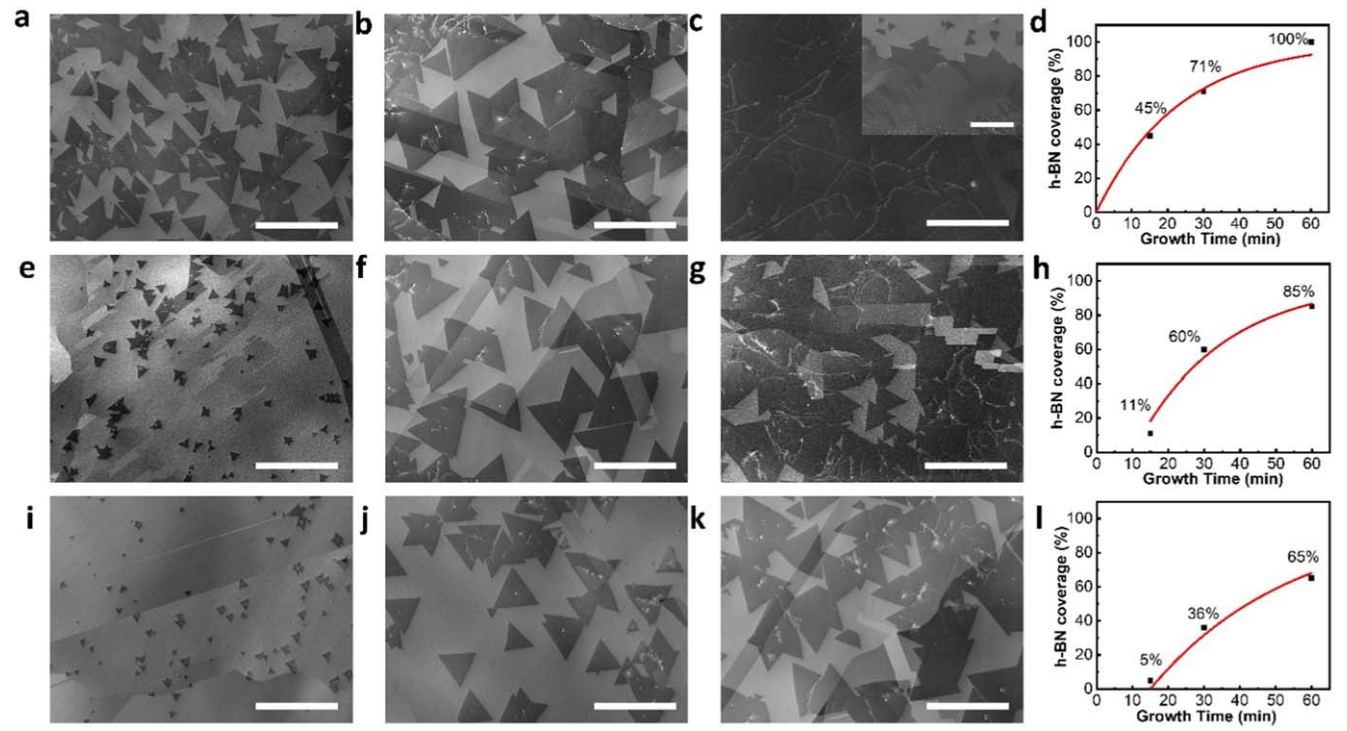

Figure 3. Morphology characterization results of time-dependent growth of h-BN monolayers. (a)–(c) SEM images of h-BN monolayer samples on Ni (111) substrates without B_2O_3 pretreatment at a growth time of 15, 30, and 60 min, respectively. (d) H-BN coverage as a function of growth time for samples shown in (a)–(c). (e)–(g) SEM images of h-BN monolayer samples on Ni (111) substrates pretreated by B_2O_3 for 30 min, at a growth time of 15, 30, and 60 min, respectively. (h) H-BN coverage as a function of growth time for samples shown in (e)–(g). (i)–(k) SEM images of h-BN monolayer samples on Ni (111) substrates pretreated by B_2O_3 for 60 min, at a growth time of 15, 30, and 60 min, respectively. (l) H-BN coverage as a function of growth time for samples shown in (i)–(k). All scale bars on SEM images are 500 μm.

where A_{BN} is the fractional coverage of h-BN, and A_0 is a constant, which is fitted to be 47.0%. t_0 is the initial time constant, which is 17 min.

Figures 3(a)–(c) show SEM images of h-BN monolayer films grown on pristine Ni (111) substrates without any B_2O_3 pretreatment at a growth time of 15, 30, and 60 min, respectively. Inset in figure 3(c) shows an SEM image of the film edge. Clear contrast in the image shows that the darker region is fully covered continuous h-BN film while the lighter region is exposed Ni substrate because this region was covered by substrate holder during the growth. The evolution of h-BN coverage versus the growth time is shown in figure 3(d), showing the increase of the coverage from 45%, to 71%, to 100%. Figures 3(e)–(g) show SEM images of h-BN monolayer films grown on 30 min B_2O_3 pretreated Ni (111) substrates at a growth time of 15, 30, and 60 min, respectively. The evolution of h-BN coverage versus the growth time is shown in figure 3(h), showing the increase of the coverage from 11%, to 60%, to 85%. Figures 3(i)–(k) show SEM images of h-BN monolayer films grown on 60 min B_2O_3 pretreated Ni (111) substrates at a growth time of 15, 30, and 60 min, respectively. The evolution of h-BN coverage versus the growth time is shown in figure 3(l), showing the increase of the coverage from 5%, to 36%, to 65%.

The overall behavior of h-BN from nucleation to film growth with coalescence and area saturation is further studied under the framework of the Johnson–Mehl–Avrami–Kolmogorov (JMAK) model [41, 48]. The modified JMAK equation is expressed as

$$A_{\mathrm{BN}} = 1 - \exp\left(k(t - t_0)\right)^n \tag{2}$$

where A_{BN} is the fractional coverage of h-BN, and k is the rate constant. The index n is the Avrami exponent, which is related to the dimensionality of the system and rates of nucleation and growth. It can be expressed as $n = qm + b$, where q equals 1 for reaction controlled linear growth, or ½ for diffusion controlled parabolic growth; m stands for the growth dimension and m is 2 for 2D growth; b stands for nucleation rate where b is 0 for site-saturated instant nucleation or b is 1 for continuous nucleation with constant rate. Figures 3(d), (h), and (l) plot the h-BN coverage versus growth time and red curves are fitted by JMAK equation. Figure S1 in the supporting information shows SEM images of more samples grown at the same condition as those in figures 3(a)–(c) but with different growth times, together with a plot of the h-BN coverage versus growth time. An average of $n = 1.05 \pm 0.02$ is extracted from these experimental data, suggesting site-saturated instant nucleation ($b \approx 0$), two-dimensional, nonlinear diffusion-controlled growth ($q \approx 1/2$, $m = 2$). Specifically, the ammonia (NH_3) and boron oxide (B_2O_3) sources were decomposed on the Ni (111) surface at growth temperature (870 °C). The decomposition supplies both boron and nitrogen atoms onto the metallic surface, leading to Ni catalyst-assisted absorption and surface diffusion of these species, and surface-mediated two-dimensional nucleation and

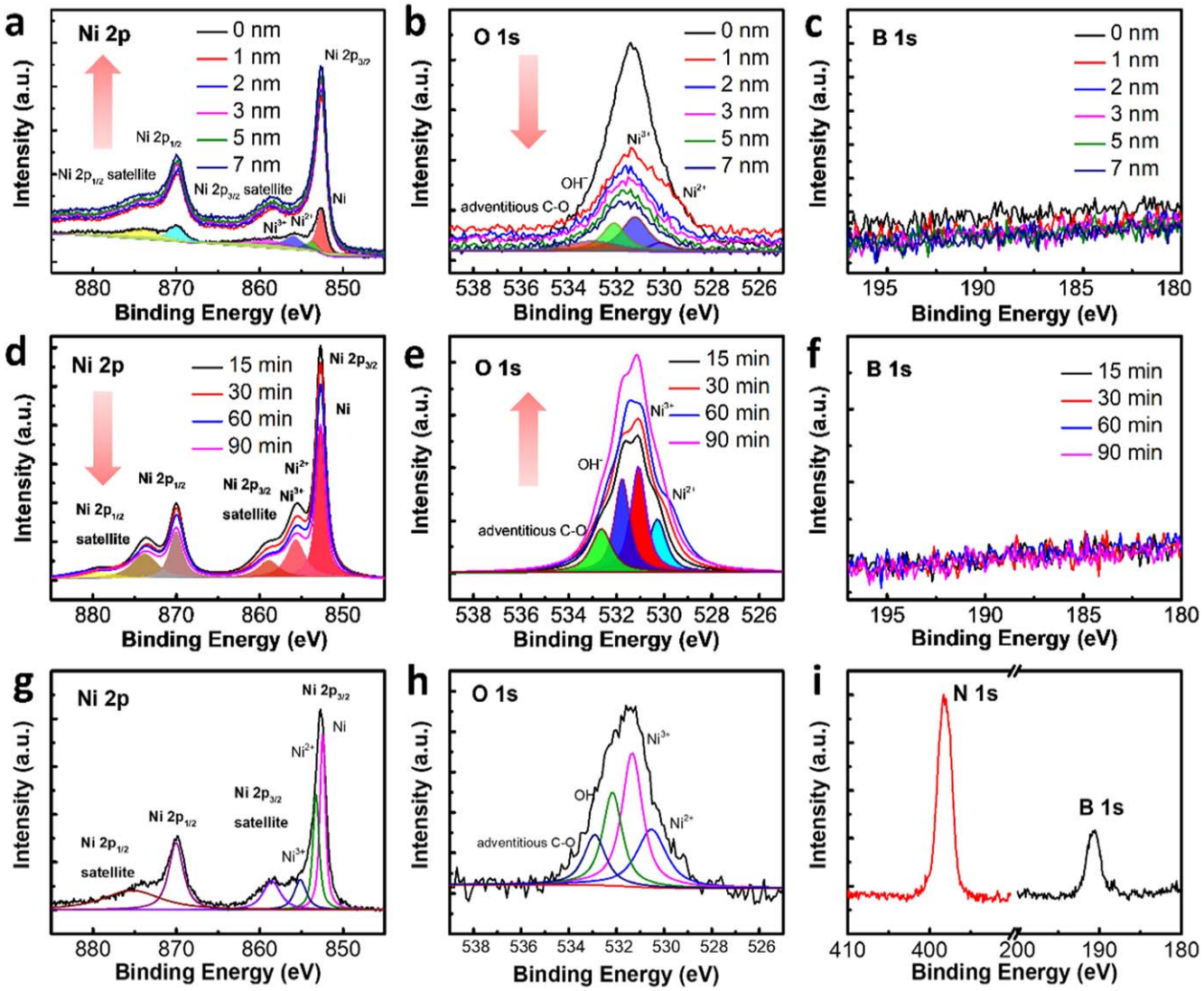

Figure 4. XPS results of Ni substrates with different B_2O_3 pretreatment times. (a)–(c) XPS sputtering depth profiling spectra of Ni 2p, O 1s, and B 1s as a function of sputtering depth from 0–7 nm from the 60 min B_2O_3 pretreated substrate surface. (d)–(f) XPS spectra showing the evolution of Ni 2p, O 1s, and B 1s from Ni substrate surfaces with different B_2O_3 pretreatment time from 15 min to 90 min. (g)–(i) XPS spectra of Ni 2p, O 1s, N 1s and B 1s from a typical as-grown h-BN sample on Ni (111) pretreated by B_2O_3 for 30 min followed by a h-BN growth duration of 30 min.

growth of h-BN films. Catalyst-assisted growth mechanism is common for the growth of 2D h-BN on all transition metal substrates. The incorporation of oxygen into Ni (111) substrate affects its catalyst strength through the change of absorption and diffusion of nitrogen and boron atoms, as presented in our DFT calculation results later.

XPS was employed to quantitatively estimate oxygen and boron bonding and concentration on the surface of Ni (111) substrates after different B_2O_3 pretreatment time and after the h-BN growth. Figures 4(a)–(c) show XPS sputtering depth profiling spectra of Ni 2p, O 1s, and B 1s as a function of sputtering depth from 0 to 7 nm from the 60 min B_2O_3 pretreated Ni (111) substrate. With the increase of sputtering depth, the overall intensity of Ni 2p peak increases while the intensity of O 1s decreases. Although the signal of B 1s peak is supposed to be located at ∼190.1 eV, there is no obvious evidence for the presence of B 1s in all depth-dependent XPS spectra. This suggests that negligible B atoms are incorporated into or stay on the Ni substrates surface, which might be due to high desorption rate of B atoms from the Ni substrate surface or boron depletion at the oxidized Ni surface [49] after pretreatment at the substrate temperature of 870 °C and without any other reactive elements such as N.

For quantitative analysis of the chemical bonding and elements states at the B_2O_3 pretreated Ni surface, the spectra of Ni 2p, O 1s and B 1s were fitted and deconvoluted as shown in figure 4. The Ni 2p spectra split in Ni $2p_{3/2}$ and Ni $2p_{1/2}$ based on the spin–orbit coupling ranging from 850 to 870 eV and from 870 to 890 eV, respectively. Complex main peaks and satellite peaks were observed from the spectra and based on their characteristic binding energy positions and areas, we can estimate the distribution of Ni and O atomic percentages and their corresponding chemical states. The structures of Ni 2p main peaks and their satellite peaks

depend on oxygen concentration and the interaction of Ni atoms with their neighboring NiO_6 octahedra [50]. The Ni 2p binding energy peaks in XPS spectra were analyzed and reported before. The Ni metal main peak in Ni $2p_{3/2}$ was reported at 852.6 eV. Binding energy peaks at 853.6, 855.3, 860.5, 866.3, 870.1, and 878.93 eV were assigned to the Ni^{2+} state and peaks at 857.2, 861.5, and 872.5 eV were assigned to Ni^{3+}. The characteristic core level of O 1s spectra in figures 4(b), (e) and (h) ranging from 525 to 539 eV can be deconvoluted into 4 peaks, O^{2-} interaction with Ni^{2+}, Ni^{3+}, OH^-, and adventitious C–O, which were located at ∼529.3, ∼531, ∼532.1, and ∼533.2 eV, respectively. The peak at ∼529.3 eV assigned to Ni^{2+} was due to the lattice oxygen interaction in the form of Ni–O octahedral bonding of NiO. The peak at ∼531 eV ascribed to Ni^{3+} was attributed to the metal vacancy or deficiency in the lattice in the form of corner-sharing NiO_4 tetrahedra. The peak at ∼532.1 eV represents the –OH group and peak at ∼533.2 eV represents the existence of adventitious C–O bond absorbed at the surface [51]. Therefore, after the pretreatment of B_2O_3, the thermodynamic equilibrium of the Ni(111) surface would form O atoms substituting the Ni vacancies [50, 52].

The Ni to O atomic ratio is estimated to increase from 0.945, 3.20, 3.69, 4.72, 6.40, to 6.80 as sputtering depth increases from 0, 1, 2, 3, 5, to 7 nm, respectively. XPS spectra in figures 4(d)–(f) show the evolution of Ni 2p, O 1s and B 1s from Ni substrate surfaces with different B_2O_3 pretreatment times, from 15, 30, 60, to 90 min. As the increase of B_2O_3 pretreatment time, Ni 2p peak intensity decreases while O 1s peak intensity increases. Based on the deconvolution estimation, the Ni to O atomic ratio is decreasing from 1.8, 1.36, 1.09, to 0.76. B 1s peak signals were not found in all these spectra as well. Thus, we attribute the dominant factor during the B_2O_3 pretreatment to the incorporation of oxygen atoms in the substrate, which influences the subsequent growth of h-BN. Figures 4(g)–(i) show XPS spectra of Ni 2p, O 1s, N 1s and B 1s obtained from one typical as-grown h-BN sample on Ni (111) pretreated by B_2O_3 for 30 min at a growth time of 30 min. The Ni to O atomic ratio of ∼1.40 after h-BN growth is slightly larger than the Ni to O atomic ratio of the pretreated substrate before h-BN growth. XPS signals from the substrate may be affected the coverage of h-BN film on surface. In addition, it also infers that during the h-BN growth, further incorporation of oxygen into Ni substrate may be limited since hydrogen species from NH_3 precursor gas and oxygen decomposed from B_2O_3 would react effectively to form H_xO species, which are pumped away. The N 1s and B 1s signals are detected around 190 eV and 397.5 eV, respectively, after h-BN growth and the N to B atomic ratio is very close to 1, suggesting the chemical stoichiometric ratio between B and N is determined to be 1/1.

Epitaxial relationship between h-BN monolayer films and oxygen-incorporated Ni (111) substrates was studied by h-BN coverage dependent reflection high-energy electron diffraction (RHEED) analysis, as shown in figure 5(a). The RHEED patterns were collected from four samples, namely, pristine high temperature annealed Ni (111) substrate, Ni (111) after pretreated by B_2O_3 for 60 min, h-BN sample of ∼50% coverage, and h-BN sample of 100% coverage. Only two sets of the RHEED patterns were observed along the $\langle 01\bar{1}0\rangle$ and $\langle 11\bar{2}0\rangle$ directions, respectively. The lattice spacings of pristine Ni (111) calculated from the RHEED pattern are 2.43 Å from the direction $\langle 01\bar{1}0\rangle$ and 4.31 Å from the direction $\langle 11\bar{2}0\rangle$. The slightly dotted patterns of pristine Ni (111) in the first column indicates the oxygen chemisorption [53, 54]. After pretreated by B_2O_3 for 60 min, the Ni (111) exhibits an expanded lattice spacings of 2.62 Å and 5.25 Å along the two directions, which might be due to the incorporation of oxygen atoms in the substrate surface. The extra strips in second column pattern from the direction $\langle 01\bar{1}0\rangle$ after pretreatment suggests the formation of NiO (111) [55] after oxygen incorporation. Then for the h-BN monolayer films with ∼50% and 100% coverage, the lattice spacings are determined to be 2.46 Å (2.47 Å) and 4.20 Å (4.20 Å), respectively. No differences in the coverage-dependent RHEED patterns and lattice spacings have been observed between h-BN and Ni (111), confirming that there was no in-plane rotation between the h-BN and Ni (111) substrate surface, further indicating the excellent epitaxial relationship and surface reconstruction during oxygen incorporation and h-BN growth process. The lattice mismatch between close-packed surface of Ni (111) (2.49 Å) and h-BN (2.50 Å) measured in our experiment was relatively very small (∼0.4%). Previous report of Raths *et al* used low energy electron diffraction (LEED) analysis presenting the very small lattice mismatch between h-BN and Ni (111) [56]. Likewise, Tonkikh *et al* reported that the in-plane lattice constant of h-BN is 2.44 ± 0.2 Å and there is a small lattice mismatch between h-BN and Ni (111) based on RHEED and HRTEM results [57].

3.2. Thermodynamics simulations of h-BN monolayer growth on oxygen incorporated Ni (111)

To understand the effect of the incorporation of oxygen atoms on the epitaxial growth of h-BN monolayers at the atomic scale, *ab initio* density functional theory (DFT) calculations using the Perdew–Burke–Ernzerhof (PBE) type generalized gradient approximation [56, 57] and the projector augmented wave (PAW) method in the Vienna *ab initio* Simulation Package (VASP) [58, 59] were carried out. Although NH_3 and B_2O_3 were used as N and B sources, a hot Ni substrate was used as a catalyst for N adatoms and decomposed H_2 or NH_x compounds. B_2O_3 was thermally decomposed to B atoms and O_2 in the effusion cell at high temperature. Therefore, B and N atoms are considered as the main reactive species on the Ni (111) substrate for the nucleation and growth of h-BN. According to the framework of the Robinson and Robins model regrading nucleation[43], the nucleation activation energy E_a is expressed as

$$E_a = E_{ads} + E_{diff} + E_{att} \quad (3)$$

where E_{ads} is the adsorption energy, E_{diff} is the energy barrier for diffusion on the substrate surface, and E_{att} is the energy barrier of attachment for capture of a surface adatom by a supercritical nucleus. A stronger catalytic effect of Ni substrate is equivalent to a lower energy barrier for the nucleation of h-BN, namely, a smaller nucleation activation energy.

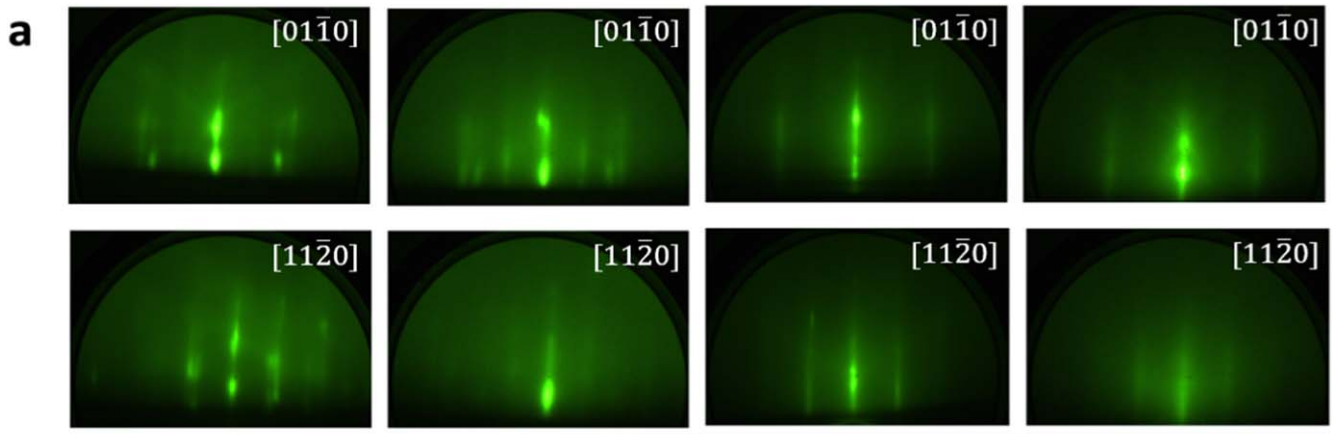

b

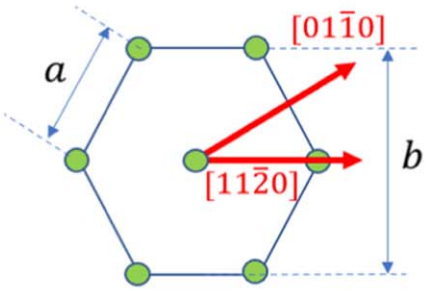

c

Lattice Parameter (Å)	[01$\bar{1}$0]	[11$\bar{2}$0]
Ni(111) Theoretical	2.49	4.32
h-BN Theoretical	2.504	4.34
Pristine Ni(111)	2.43	4.31
After B_2O_3 treatment	2.62	5.25
h-BN Partial (50%) coverage	2.46	4.20
h-BN 100% coverage	2.47	4.20

Figure 5. (a) RHEED patterns of pristine Ni (111) substrate, Ni (111) after pretreated by B_2O_3 for 60 min, h-BN sample of ∼50% coverage, and h-BN sample of 100% coverage from left to right. Two sets of RHEED patterns along [01$\bar{1}$0] and [11$\bar{2}$0] are shown in the two rows. (b) Schematic showing that two sets of patterns were observed from direction [01$\bar{1}$0] and [11$\bar{2}$0]. (c) A summary table showing the theoretical and measured lattice spacings from direction [01$\bar{1}$0] and [11$\bar{2}$0].

Also, the nucleation density N_s can be expressed as [60–62]

$$N_s \propto N_{s0} \exp\left(-\frac{E_a}{kT}\right) \tag{4}$$

where N_{S0} is a pre-exceptional term, which is related to the impinging rate of B/N atoms onto the surface and the density of nucleation sites, k is the Boltzmann constant, and T is the temperature.

At a given temperature and source flux, the increase of adsorption, diffusion, and attachment energies can suppress the nucleation of h-BN. Here, we investigate how the oxygen atoms incorporated into the Ni (111) substrate change these energies, leading to the eventual nucleation and growth of h-BN. The absorption energies of B and N atoms on the Ni substrate can be expressed as

$$E_{\text{ads}} = E_{\text{B/Non surface}} - E_{\text{B/N}} - E_{\text{surface}} \tag{5}$$

where $E_{\text{B/N}}$ is the energy of the isolated B and N atoms, E_{surface} is the energy of the clean Ni surface without the absorbents, and $E_{\text{B/Non surface}}$ is the total energy of the Ni surface with the B and N adsorbates. A lower adsorption energy E_{ads} indicates a more stable adsorption state. Five different adsorption sites were calculated, namely, HCP, TOP, FCC, Bridge, and HCP_{adj} sites. Figure 6(a) shows schematic of three Ni (111) surfaces investigated here, i.e. pristine Ni (111) and Ni (111) with one or two embedded substitutional oxygen atoms at the surface site in the 4 × 4 × 4 slab models. Figure 6(b) shows the DFT calculation results of these adsorption energies on these Ni (111) surfaces. In the presence of substitutional O, the adsorption energies of B and N are reduced at most of the sites, such as at HCP, FCC, and HCP_{adj}, indicating the more favorable and stable substitutional oxygen point defects in the adsorption process [63, 64].

The effect of substitutional oxygen on the diffusion activation energy (E_{diff}) of B and N atoms was calculated using the climbing image nudged elastic band (CI-NEB) method. Figures 6(c) and (d) show the CI-NEB diffusion energy profiles of B and N versus adsorption sites. The diffusion path of B and N atoms, as shown in figure 6(a), is from an HCP site, through a TOP site, a FCC, and a Bridge site, and to an adjacent HCP site. The black lines show the energies along the path on the pristine surface, the red lines are energy profiles with one oxygen atom embedded, and the blue lines are the energy profiles with two oxygen atoms embedded. With the presence and increase of embedded oxygen amount, the energy barriers of B and N diffusion from an HCP site to the adjacent HCP site are increased, indicating the adverse effect of oxygen incorporation on the diffusion process. The increase in barrier height for diffusion of nitrogen and boron atoms on oxygen incorporated Ni (111) surface due to the increase of oxygen incorporation in the pristine Ni surface leads to the adverse effect on the diffusion of the boron and nitrogen atoms, thus explaining the slower growth speed of the h-BN monolayers in the experiment. Similar

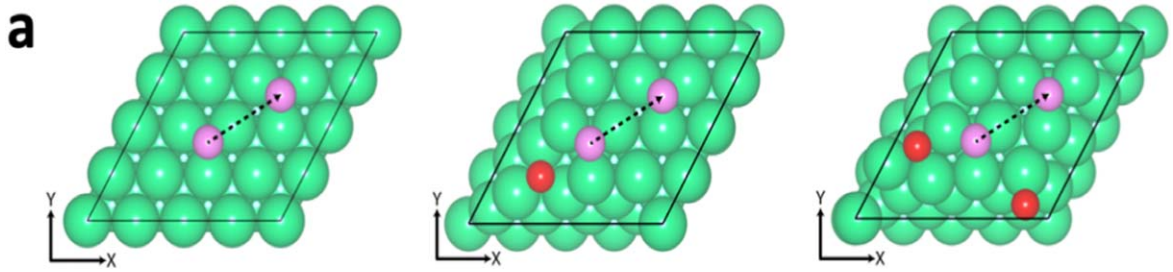

b

Adsorption Energy eV/atom	HCP	TOP	FCC	BRIDGE	HCP_{adj}
B (Pristine)	1.84	3.75	1.93	1.95	1.84
1O-B	1.81	3.74	1.93	1.98	1.86
2O-B	-1.68	3.85	-0.59	-0.95	-1.39
N (Pristine)	-2.14	0.66	-2.17	-1.77	-2.14
1O-B	-2.40	0.67	-2.18	-1.67	-2.09
2O-B	-5.21	0.89	-4.77	-4.70	-5.55

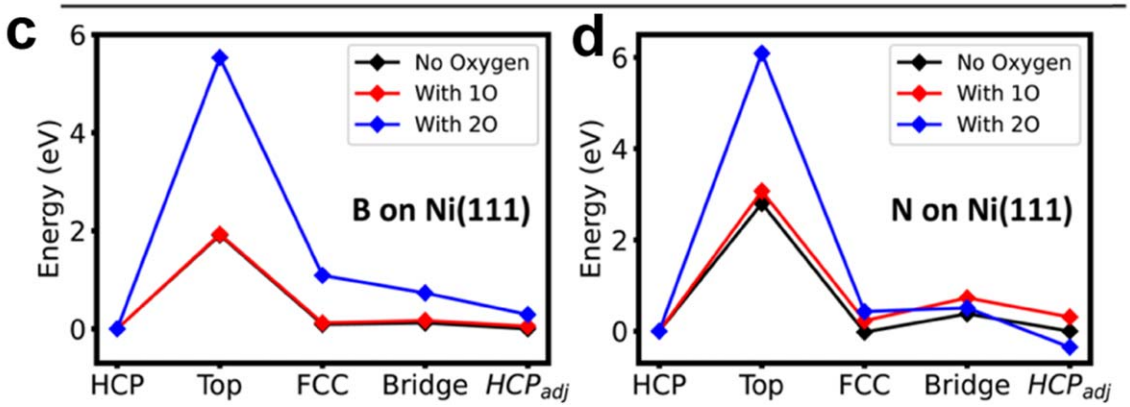

Figure 6. Theoretical calculation results of adsorption and diffusion energies of B and N atoms on pristine Ni (111) without oxygen incorporation (pristine), Ni (111) with one substitutional oxygen atom incorporation (1O), and Ni (111) with two substitutional oxygen atoms incorporation (2O) on the surface. (a) Top view of three kinds of substrates, pristine, 1O, and 2O, with B or N atoms on top. The diffusion path of B or N atom from an HCP site to an adjacent HCP site is also indicated. (b) DFT calculated adsorption energies of B and N on the three substrates. Diffusion energy profiles of (c) B, and (d) N on the three substrates diffusing along the paths indicated in (a).

studies of the effect of the incorporation of carbon atoms in Co and Ni on the growth of 2D h-BN films have been reported elsewhere [3, 39, 41, 63, 64].

Since the attachment energy E_{att} is related to the attachment of adatom to nucleus, it shall be the same for the h-BN growth on Ni (111) with or without oxygen incorporation. Although absorption energies are somewhat decreased, the diffusion barriers are increased relatively more after the incorporation of oxygen. Thus, the overall nucleation energy as a sum of these energies per equation (3) is increased, leading to less nucleation density per equation (4) and slower growth, which is in good agreement with the experimental results shown above. It should be noted that while embedding oxygen atoms in Ni (111) as substitutional atoms is proved here to inhibit the growth of 2D h-BN, the incorporation of oxygen atoms in copper has increased the growth of 2D h-BN [46, 47]. Although no detailed DFT analysis was given to explain their results in these reports [46, 47], we hypothesize that the catalytic strength of copper is enhanced after oxygen incorporation.

3.3. Structural, optical, and electrical properties of h-BN monolayers grown on oxygen incorporated Ni (111)

Figure 7(a) shows dark-field optical microscope image of as-grown h-BN flakes on Ni (111) substrate pretreated by B_2O_3 for 30 min at a growth time of 30 min. The dark triangular regions are h-BN flakes detected by the light scattering at the thin film edges. Figure 7(b) shows UV–vis absorption spectrum obtained from an h-BN film transferred onto a sapphire

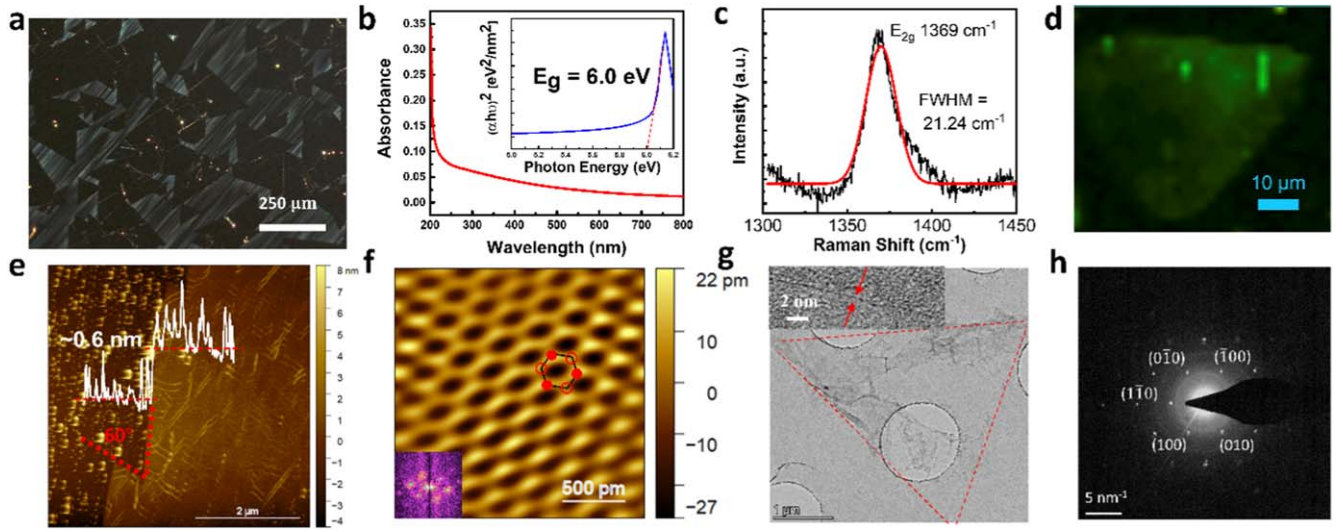

Figure 7. Characterization results of h-BN monolayer. (a) Dark-field optical microscope image of h-BN flakes grown on Ni (111) substrate. (b) UV visible absorption spectrum of transferred h-BN film on sapphire substrate. Inset is its Tauc plot, indicating the optical bandgap ~6 eV. (c) Typical Raman spectrum of h-BN film transferred onto the SiO_2 wafer. Peak 1369 cm^{-1} indicates the in-plane E_{2g} vibration mode of hexagonal B–N bonds. (d) Raman mapping of a triangular h-BN domain. (e) AFM image scanned across the h-BN film edge, showing the step height ~0.6 nm, indicating the existence of monolayer. (f) STM image of as-grown monolayer h-BN film on Ni (111) substrate. (g) TEM image of the transferred h-BN film onto a copper TEM grid coated with c-flat holy carbon film. Dash lines show the triangular shape of the transferred film. Inset is the cross-sectional HRTEM image of the folded / curled edge of the transferred film, also indicating the existence of h-BN monolayer. (h) SAED pattern of the h-BN film.

substrate. The inset in figure 7(b) is the Tauc plot of the absorption spectrum, showing that the optical band gap of h-BN is ~ 6 eV [65]. Figure 7(c) shows Raman spectra obtained from an h-BN film transferred on a SiO_2/Si wafer. The high-quality h-BN film has the peak with the full width at half maximum (FWHM) ~21.24 cm^{-1} located around 1369 cm^{-1}, which corresponds to the E_{2g} vibration mode of B–N bonds, implying the existence of monolayer. Figure 7(d) shows the Raman mapping of a triangular single crystal h-BN domain, with uniform E_{2g} signal across the whole domain.

The roughness and thickness of h-BN film was measured by atomic force microscopy (AFM) from a PMMA-assisted transferred h-BN film on a SiO_2/Si wafer as shown in figure 7(e). The undulating line scanning profile in figure 7(e) across the film edge from the inset is attributed to the PMMA residues during the film transfer, but the step height of around 0.6 nm can be extracted. The larger experimental value compared to the theoretical value (~0.33 nm) is a result of AFM cantilever tip effects including the different van der Waals force between h-BN and SiO_2 surface at the tip-surface interface. Figures S2(a)–(d) show additional AFM images of the transferred h-BN film. The 60° zig-zag edges of h-BN are retained after transfer shown in figures 7(e) and S2(a)–(c), and the triangular shapes are nitrogen terminated edges due to energetic preference [66, 67]. Larger scale 10 × 10 μm^2 AFM image in figure S2(d) shows the extreme flat (RMS roughness ~1.063 nm) surface of the transferred h-BN film with the existence of wrinkles, which may be induced during the growth and cooling process.

Figure 7(f) shows a scanning tunneling microscopy (STM) image of as-grown h-BN sample in figure 7(a). Positive voltage was applied to the Pt–Ir tip; therefore, only nitrogen atoms were resolved. The brighter nodes in the hexagonal network indicated by red solid circles represent nitrogen atoms, while the dimmer nodes indicated by red hollow circles represent boron atoms. The average N to adjacent N atom distance was measured to be ~2.5 Å, which is very close to the theoretical value. Inset shows the fast Fourier transform of the STM image and the six spots in a hexagonal shape correspond to the reciprocal lattice of h-BN. Figure S3 in supporting information shows a large-area (10 m × 10 nm) atomic resolution STM image of as-grown monolayer h-BN on Ni (111) substrate. The RMS roughness under this scale is ~40.55 pm. The slightly corrugated surface is due to the epitaxial growth of h-BN on reconstructed Ni (111) surface with nano steps and terrain. Figure 7(g) shows plane view TEM image of one h-BN flake transferred onto a copper TEM grid coated with holey carbon film. The inset shows the cross-sectional HRTEM image of the folded or curled h-BN film edge, revealing that the large h-BN domain is monolayer. The single crystal crystallinity is confirmed by selected area electron diffraction (SAED) pattern in figure 7(h), where the spot-to-spot distance in reciprocal space pattern converted to real space lattice constant matches the theoretical value of single crystal h-BN.

Figure 8 shows the electrical characterization results from the fabricated metal–insulator–metal (MIM) devices on an as-grown continuous single-crystal h-BN monolayer film pre-treated by B_2O_3 for 30 min at a growth time of 90 min. Figure 8(a) shows a bright-field optical microscope image of the fabricated devices with different electrode sizes, 50 × 50, 100 × 100, 150 × 150, 200 × 200, and 250 × 250 μm^2, respectively. Inset is the schematic of the structure of the Al/monolayer h-BN/Ni devices, where Al is the top electrode,

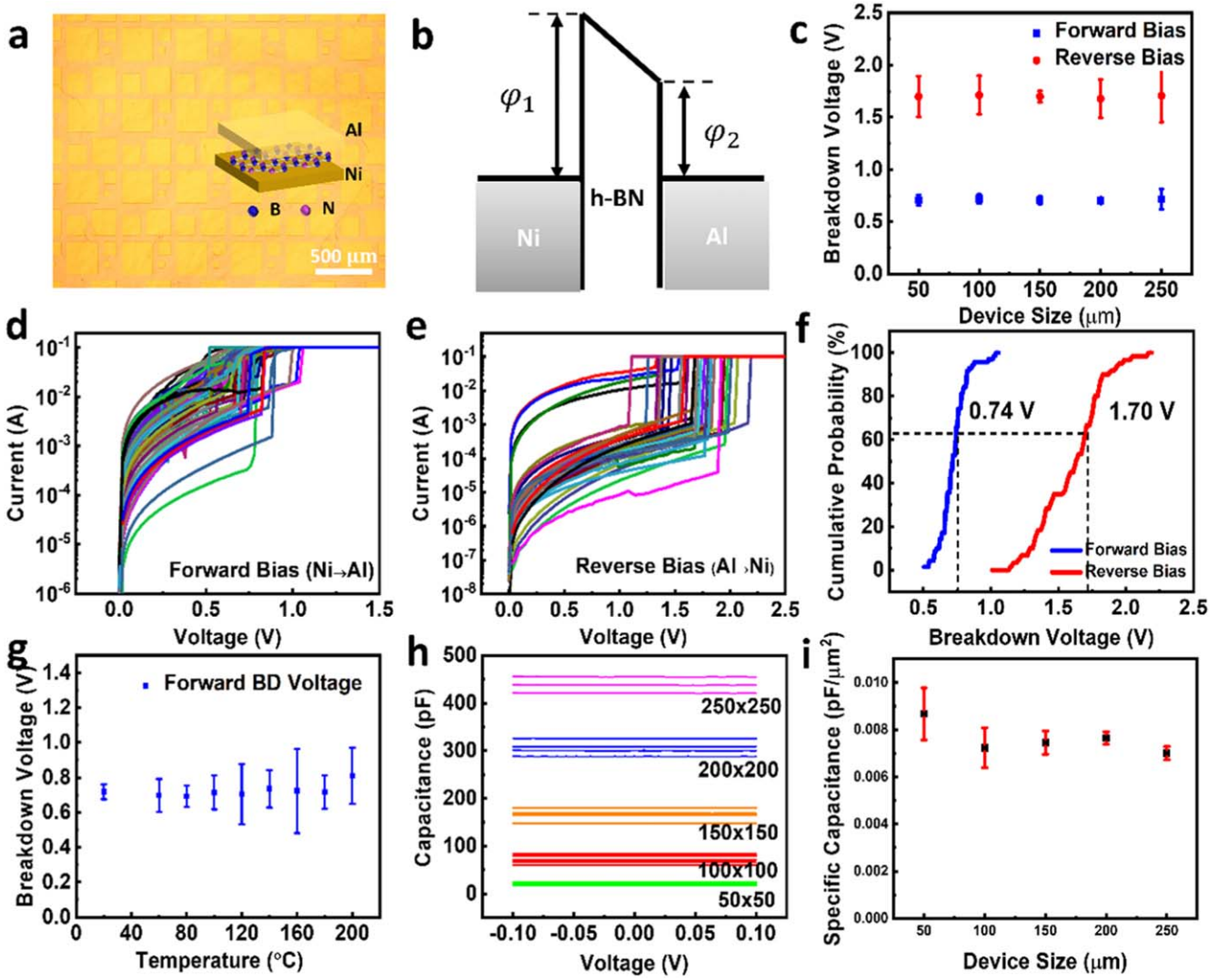

Figure 8. Characterization results of fabricated h-BN monolayer MIM devices. (a) Optical microscope image of the MIM devices with different sizes, 50 × 50, 100 × 100, 150 × 150, 200 × 200, and 250 × 250 μm^2. Inset shows a schematic of an Al/h-BN/Ni device structure. (b) Band diagram of the MIM structure at thermal equilibrium. (c) Forward and reverse breakdown voltages of MIM devices with different device sizes. (d) Multiple forward *I–V* characteristics of Ni/h-BN/Al with device size of 250 × 250 μm^2. (e) Multiple reverse *I–V* characteristics of Al/h-BN/Ni with device size of 250 × 250 μm^2. (f) Cumulative probability distribution of breakdown voltages. (g) Temperature-dependent forward breakdown of 100 × 100 μm^2 Ni/h-BN/Al devices, from room temperature to 200 °C. (h) *C–V* characteristics at 100 kHz of Ni/h-BN/Al devices with size of 50 × 50, 100 × 100, 150 × 150, 200 × 200, and 250 × 250 μm^2. (i) Specific capacitance of capacitors of different sizes.

and the bottom Ni electrode is the Ni (111) substrate. The top square-shaped metal contact was fabricated by photolithography and e-beam evaporation, where 100 nm thick Al layer was deposited. Figure 8(b) shows the schematic of energy band diagram of the Al/h-BN/Ni structure at thermal equilibrium, where φ_1 and φ_2 are the barrier heights of Ni/h-BN and Al/h-BN junctions, where $\varphi_1(\sim 5.1\text{eV})$ is around 0.9 eV larger than $\varphi_2(\sim 4.2\text{eV})$ in theory [68, 69]. The work function difference between Ni and Al results in a built-in potential across the monolayer h-BN layer. Here, forward bias is designated as positive voltage being applied on the top Al electrode, and reverse bias is vice versa. Figure 8(c) shows the forward and reverse breakdown voltages of the devices with different sizes. As seen from the figure, forward breakdown voltage is about 0.96 V smaller than reverse breakdown voltage. In addition, both forward and reverse breakdown voltages of different sizes are very similar, respectively, implying that electrical breakdown behavior is independent of the electrode area. Figure 8(d) shows multiple forward *I–V* characteristics in the 250 × 250 μm^2 devices with a compliance current of 100 mA. Figure 8(e) shows multiple reverse *I–V* characteristics in the 250 × 250 μm^2 devices with a compliance current of 100 mA. Direct tunneling characteristics with breakdown are evident in both cases. The cumulative probability distribution of forward and reverse breakdown voltages in figures 8(d) and (e) are summarized in figure 8(f). By setting the probability to 0.63 according to the Weibull distribution [16, 70, 71], the estimated forward and reverse breakdown voltages are 0.74 V and 1.70 V, respectively. The difference of the absolute values

($V_{reverse} - V_{forward} \approx 0.96V$) is attributed to the built-in voltage at equilibrium across the h-BN, which is in good agreement with the theoretical values. High breakdown electric field is calculated to be $\sim$11.2 MV cm^{-1} based on 0.74 V breakdown voltage and atomic distance between two metal electrodes separated by h-BN monolayer [5]. Figure 8(g) shows the temperature-dependent forward breakdown characteristics in the 100 $\times$ 100 μm^2 devices with a compliance current of 100 mA from room temperature (25 °C) to 200 °C. The distribution of voltages is very uniform with the increase of the temperatures, indicating that the electrical breakdown is independent of temperature.

Figure 8(h) shows capacitance–voltage (C–V) characteristics of the MIM nanocapacitors at 100 kHz with different sizes of 50 $\times$ 50, 100 $\times$ 100, 150 $\times$ 150, 200 $\times$ 200, and 250 $\times$ 250 μm^2, respectively. The specific capacitance of these capacitors of different sizes are summarized in figure 8(i) with great distribution consistency. The smaller measured average specific capacitance of 0.008 pFμm^{-2} than theoretical geometric capacitance of 0.087 pFμm^{-2} is attributed to series capacitances from geometric capacitance (C_g) and vacuum capacitance (C_v), which is due to extra geometric distance between two electrodes from van der Waals interaction of the interface between the h-BN and metal electrodes [72], and vacuum layer from surface corrugation and reconstruction [5, 73–77], respectively.

4. Conclusions

The role of embedding oxygen atoms in the transition Ni (111) substrates on the growth of h-BN monolayers has been studied. By treating the Ni (111) substrate with the exposure to B_2O_3 at a temperature of 870 °C, the adverse effect of oxygen atoms incorporation into Ni (111) substrates on the growth of h-BN monolayers were found, and the more incorporation of oxygen atoms in the substrates, the greater inhibition of the epitaxial growth of h-BN on the Ni (111) surface. DFT and CI-NEB calculations reveal that the diffusion of B and N atoms on Ni (111) are suppressed by embedded substitutional oxygen atoms. Large-area epitaxial single-crystal h-BN monolayer films were obtained. MIM devices based on the as-grown h-BN monolayer film were fabricated, and the electrical breakdown and nano-capacitance were studied, which demonstrate the high quality of the MBE grown single-layer h-BN films. Our work provides a better understanding of the great influence of heterogeneous catalysis through transition metal substrate engineering or modification on the reliable synthesis of high-quality, large-area, single crystal monolayer h-BN films for various applications. A similar strategy can also be adopted for the synthesis of other 2D crystalline materials.

Acknowledgments

This work was supported by the UCR Foundation and UCR Academic Senate Committee on Research grant. The work used STAMPEDE2 at TACC through allocation DMR130081 from the Advanced Cyberinfrastructure Coordination Ecosystem: Services and Support (ACCESS) program, which is supported by National Science Foundation grants #2138259, #2138286, #2138307, #2137603, and #2138296. J T and P W would like to acknowledge NSF under award NSF CAREER-2046648. This work was partially supported by the Office of Postsecondary Education through the award GAANN Fellows in Materials Science and Engineering #P200A210031.

Data availability statement

All data that support the findings of this study are included within the article (and any supplementary files).

Supporting information

H-BN growth condition and modelling; nano-characterization of h-BN samples.

ORCID iDs

Yuan Li https://orcid.org/0000-0002-8898-0407
Yanwei He https://orcid.org/0000-0001-7544-6160
Tianchen Yang https://orcid.org/0000-0002-0991-471X
Jianlin Liu https://orcid.org/0000-0001-6513-0867

References

[1] Cassabois G, Valvin P and Gil B 2016 Hexagonal boron nitride is an indirect bandgap semiconductor *Nat. Photon.* **10** 262–6
[2] Wang L *et al* 2019 Epitaxial growth of a 100 square-centimetre single-crystal hexagonal boron nitride monolayer on copper *Nature* **570** 91–5
[3] He Y *et al* 2020 Growth of high-quality hexagonal boron nitride single-layer films on carburized ni substrates for metal–insulator–metal tunneling devices *ACS Appl. Mater. Interfaces* **12** 35318–27
[4] Song L *et al* 2010 Large scale growth and characterization of atomic hexagonal boron nitride layers *Nano Lett.* **10** 3209–15
[5] He Y *et al* 2021 Robust nanocapacitors based on wafer-scale single-crystal hexagonal boron nitride monolayer films *ACS Appl. Nano Mater.* **4** 5685–95
[6] Wang J I-J *et al* 2022 Hexagonal boron nitride as a low-loss dielectric for superconducting quantum circuits and qubits *Nat. Mater.* **21** 398–403
[7] Stolyarov M A, Liu G, Rumyantsev S L, Shur M and Balandin A A 2015 Suppression of 1/f noise in near-ballistic h-BN-graphene-h-BN heterostructure field-effect transistors *Appl. Phys. Lett.* **107** 023106
[8] Wang J *et al* 2016 High mobility MoS_2 transistor with low schottky barrier contact by using atomic thick h-BN as a tunneling layer *Adv. Mater.* **28** 8302–8
[9] Jang S K, Youn J, Song Y J and Lee S 2016 Synthesis and characterization of hexagonal boron nitride as a gate dielectric *Sci Rep.* **6** 30449

[10] Sasama Y, Komatsu K, Moriyama S, Imura M, Teraji T, Watanabe K, Taniguchi T, Uchihashi T and Takahide Y 2018 High-mobility diamond field effect transistor with a monocrystalline h-BN gate dielectric *APL Mater.* **6** 111105

[11] Kang Kim K, Seok Lee H and Hee Lee Y 2018 Synthesis of hexagonal boron nitride heterostructures for 2D van der waals electronics *Chem. Soc. Rev.* **47** 6342–69

[12] Pan C *et al* 2017 Coexistence of grain-boundaries-assisted bipolar and threshold resistive switching in multilayer hexagonal boron nitride *Adv. Funct. Mater.* **27** 1604811

[13] Zhu K, Liang X, Yuan B, Villena M A, Wen C, Wang T, Chen S, Hui F, Shi Y and Lanza M 2019 Graphene–boron nitride–graphene cross-point memristors with three stable resistive states *ACS Appl. Mater. Interfaces* **11** 37999–8005

[14] Jing X, Puglisi F, Akinwande D and Lanza M 2019 Chemical vapor deposition of hexagonal boron nitride on metal-coated wafers and transfer-free fabrication of resistive switching devices *2D Mater.* **6** 035021

[15] Yuan B *et al* 2020 150 nm × 200 nm cross-point hexagonal boron nitride-based memristors *Adv. Electron. Mater.* **6** 1900115

[16] Li Y, Cui Z, He Y, Tian H, Yang T, Shou C and Liu J 2022 Resistive switching properties of monolayer h-BN atomristors with different electrodes *Appl. Phys. Lett.* **120** 173104

[17] Tran T T, Elbadawi C, Totonjian D, Lobo C J, Grosso G, Moon H, Englund D R, Ford M J, Aharonovich I and Toth M 2016 Robust multicolor single photon emission from point defects in hexagonal boron nitride *ACS Nano* **10** 7331–8

[18] Shotan Z, Jayakumar H, Considine C R, Mackoit M, Fedder H, Wrachtrup J, Alkauskas A, Doherty M W, Menon V M and Meriles C A 2016 Photoinduced modification of single-photon emitters in hexagonal boron nitride *ACS Photon.* **3** 2490–6

[19] Sajid A, Ford M J and Reimers J R 2020 Single-photon emitters in hexagonal boron nitride: a review of progress *Rep. Prog. Phys.* **83** 044501

[20] Dean C R *et al* 2010 Boron nitride substrates for high-quality graphene electronics *Nat. Nanotech* **5** 722–6

[21] Bresnehan M S, Hollander M J, Wetherington M, LaBella M, Trumbull K A, Cavalero R, Snyder D W and Robinson J A 2012 Integration of hexagonal boron nitride with quasi-freestanding epitaxial graphene: toward wafer-scale, high-performance devices *ACS Nano* **6** 5234–41

[22] Li T, Tang Z, Huang Z and Yu J 2018 Substrate effects on the thermal performance of in-plane graphene/hexagonal boron nitride heterostructures *Carbon* **130** 396–400

[23] Yankowitz M, Xue J and LeRoy B J 2014 Graphene on hexagonal boron nitride *J. Phys. Condens. Matter* **26** 303201

[24] Yamoah M A, Yang W, Pop E and Goldhaber-Gordon D 2017 High-velocity saturation in graphene encapsulated by hexagonal boron nitride *ACS Nano* **11** 9914–9

[25] Auwärter W 2019 Hexagonal boron nitride monolayers on metal supports: versatile templates for atoms, molecules and nanostructures *Surf. Sci. Rep.* **74** 1–95

[26] Novoselov K S, Geim A K, Morozov S V, Jiang D, Zhang Y, Dubonos S V, Grigorieva I V and Firsov A A 2004 Electric field effect in atomically thin carbon films *Science* **306** 666–9

[27] Lin Y, Williams T V and Connell J W 2010 Soluble, exfoliated hexagonal boron nitride nanosheets *J. Phys. Chem. Lett.* **1** 277–83

[28] Li X, Hao X, Zhao M, Wu Y, Yang J, Tian Y and Qian G 2013 Exfoliation of hexagonal boron nitride by molten hydroxides *Adv. Mater.* **25** 2200–4

[29] L. Marsh K, Souliman M and B. Kaner R 2015 Co-solvent exfoliation and suspension of hexagonal boron nitride *Chem. Commun.* **51** 187–90

[30] Wang N, Yang G, Wang H, Yan C, Sun R and Wong C-P 2019 A universal method for large-yield and high-concentration exfoliation of two-dimensional hexagonal boron nitride nanosheets *Mater. Today* **27** 33–42

[31] Chugh D, Wong-Leung J, Li L, Lysevych M, Tan H H and Jagadish C 2018 Flow modulation epitaxy of hexagonal boron nitride *2D Mater.* **5** 045018

[32] Gibb A L, Alem N, Chen J-H, Erickson K J, Ciston J, Gautam A, Linck M and Zettl A 2013 Atomic resolution imaging of grain boundary defects in monolayer chemical vapor deposition-grown hexagonal boron nitride *J. Am. Chem. Soc.* **135** 6758–61

[33] Li Q, Zou X, Liu M, Sun J, Gao Y, Qi Y, Zhou X, Yakobson B I, Zhang Y and Liu Z 2015 Grain boundary structures and electronic properties of hexagonal boron nitride on Cu(111) *Nano Lett.* **15** 5804–10

[34] Lu J, Yeo P S E, Zheng Y, Xu H, Gan C K, Sullivan M B, Castro Neto A H and Loh K P 2013 Step flow versus mosaic film growth in hexagonal boron nitride *J. Am. Chem. Soc.* **135** 2368–73

[35] Tang S, Ding G, Xie X, Chen J, Wang C, Ding X, Huang F, Lu W and Jiang M 2012 Nucleation and growth of single crystal graphene on hexagonal boron nitride *Carbon* **50** 329–31

[36] Lee J S *et al* 2018 Wafer-scale single-crystal hexagonal boron nitride film via self-collimated grain formation *Science* **362** 817–21

[37] Chen T-A *et al* 2020 Wafer-scale single-crystal hexagonal boron nitride monolayers on Cu (111) *Nature* **579** 219–23

[38] Cheng T S, Summerfield A, Mellor C J, Davies A, Khlobystov A N, Eaves L, Foxon C T, Beton P H and Novikov S V 2018 High-temperature molecular beam epitaxy of hexagonal boron nitride layers *J. Vac. Sci. Technol.* B **36** 02D103

[39] Tian H, He Y, Das P, Cui Z, Shi W, Khanaki A, Lake R K and Liu J 2019 Growth dynamics of millimeter-sized single-crystal hexagonal boron nitride monolayers on secondary recrystallized Ni (100) substrates *Adv. Mater. Interfaces* **6** 1901198

[40] He Y, Tian H, Khanaki A, Shi W, Tran J, Cui Z, Wei P and Liu J 2019 Large-area adlayer-free single-layer h-BN film achieved by controlling intercalation growth *Appl. Surf. Sci.* **498** 143851

[41] Tian H, Khanaki A, Das P, Zheng R, Cui Z, He Y, Shi W, Xu Z, Lake R and Liu J 2018 Role of carbon interstitials in transition metal substrates on controllable synthesis of high-quality large-area two-dimensional hexagonal boron nitride layers *Nano Lett.* **18** 3352–61

[42] Khanaki A, Tian H, Xu Z, Zheng R, He Y, Cui Z, Yang J and Liu J 2017 Effect of high carbon incorporation in Co substrates on the epitaxy of hexagonal boron nitride/graphene heterostructures *Nanotechnology* **29** 035602

[43] Caneva S, Weatherup R S, Bayer B C, Brennan B, Spencer S J, Mingard K, Cabrero-Vilatela A, Baehtz C, Pollard A J and Hofmann S 2015 Nucleation control for large, single crystalline domains of monolayer hexagonal boron nitride via Si-doped Fe catalysts *Nano Lett.* **15** 1867–75

[44] Shi Z, Lu G, Yang P, Wu T, Yin W, Zhang C, Jiang R and Xie X 2019 Controlled synthesis of uniform multilayer hexagonal boron nitride films on Fe_2B alloy *RSC Adv.* **9** 10155–8

[45] Liu S, He R, Ye Z, Du X, Lin J, Jiang H, Liu B and Edgar J H 2017 Large-scale growth of high-quality hexagonal boron nitride crystals at atmospheric pressure from an Fe–Cr Flux *Cryst. Growth Des.* **17** 4932–5

[46] Chang R-J, Wang X, Wang S, Sheng Y, Porter B, Bhaskaran H and Warner J H 2017 Growth of large single-crystalline monolayer hexagonal boron nitride by oxide-assisted chemical vapor deposition *Chem. Mater.* **29** 6252–60
[47] Malik M W, Ullah S, Wang B, Jaddi S, Zeng Y and Raskin J-P 2023 Oxygen activated CVD growth of large-area multilayer h-BN on polycrystalline copper foils *J. Cryst. Growth* **606** 127088
[48] Kim H, Mattevi C, Calvo M R, Oberg J C, Artiglia L, Agnoli S, Hirjibehedin C F, Chhowalla M and Saiz E 2012 Activation energy paths for graphene nucleation and growth on Cu *ACS Nano* **6** 3614–23
[49] Jalowicka A, Nowak W, Young D J, Nischwitz V, Naumenko D and Quadakkers W J 2015 Boron depletion in a nickel base superalloy induced by high temperature oxidation *Oxid. Met.* **83** 393–413
[50] Salunkhe P, Muhammed A A V and Kekuda D 2020 Investigation on tailoring physical properties of nickel oxide thin films grown by dc magnetron sputtering *Mater. Res. Express* **7** 016427
[51] Grosvenor A P, Biesinger M C, Smart R, St C and McIntyre N S 2006 New interpretations of XPS spectra of nickel metal and oxides *Surf. Sci.* **600** 1771–9
[52] Islam R, Chen G, Ramesh P, Suh J, Fuchigami N, Lee D, Littau K A, Weiner K, Collins R T and Saraswat K C 2017 Investigation of the changes in electronic properties of nickel oxide (NiO*x*) Due to UV/Ozone treatment *ACS Appl. Mater. Interfaces* **9** 17201–7
[53] Narusawa T, Gibson W M and Törnqvist E 1982 Structure study of oxygen-adsorbed Ni(111) surface by high energy ion scattering *Surf. Sci.* **114** 331–48
[54] Dolle P, Alnot M, Ehrhardt J J, Thomy A and Cassuto A 1985 Photoemission of physisorbed Xe as a probe of Ni(111) oxidation under low pressure *Surf. Sci.* **152–153** 620–6
[55] Okazawa T, Nishizawa T, Nishimura T and Kido Y 2007 Oxidation kinetics for Ni (111) and the structure of the oxide layers *Phys. Rev.* **75** 033413 B
[56] Raths M, Schott C, Knippertz J, Franke M, Lin Y-R, Haags A, Aeschlimann M, Kumpf C and Stadtmüller B 2021 Growth, domain structure, and atomic adsorption sites of hBN on the Ni(111) surface *Phys. Rev. Mater.* **5** 094001
[57] Tonkikh A A, Voloshina E N, Werner P, Blumtritt H, Senkovskiy B, Güntherodt G, Parkin S S P and Dedkov Y S 2016 Structural and electronic properties of epitaxial multilayer h-BN on Ni(111) for spintronics applications *Sci Rep.* **6** 23547
[58] Ernzerhof M and Scuseria G E 1999 Assessment of the perdew–burke–ernzerhof exchange-correlation functional *J. Chem. Phys.* **110** 5029–36
[59] Perdew J P, Burke K and Ernzerhof M 1996 Generalized gradient approximation made simple *Phys. Rev. Lett.* **77** 3865–8
[60] Kresse G and Hafner J 1993 *Ab initio* molecular dynamics for liquid metals *Phys. Rev.* B **47** 558–61
[61] Kresse G and Furthmüller J 1996 Efficiency of ab-initio total energy calculations for metals and semiconductors using a plane-wave basis set *Comput. Mater. Sci.* **6** 15–50
[62] Lewis B and Campbell D S 1967 Nucleation and initial-growth behavior of thin-film deposits *J. Vac. Sci. Technol.* **4** 209–18
[63] Robinson V N E and Robins J L 1974 Nucleation kinetics of gold deposited onto UHV cleaved surfaces of NaCl and KBr *Thin Solid Films* **20** 155–75
[64] Ratsch C and Venables J A 2003 Nucleation theory and the early stages of thin film growth *J. Vac. Sci. Technol.* A **21** S96–109
[65] Xing H, Hu P, Li S, Zuo Y, Han J, Hua X, Wang K, Yang F, Feng P and Chang T 2021 Adsorption and diffusion of oxygen on metal surfaces studied by first-principle study: a review *J. Mater. Sci. Technol.* **62** 180–94
[66] Zenia H, Lounis K, Megchiche E H and Mijoule C 2016 Stability of vacancy-oxygen complexes in bulk nickel: atomistic and *ab initio* calculations *Comput. Mater. Sci.* **124** 428–37
[67] Henkelman G, Uberuaga B P and Jónsson H 2000 A climbing image nudged elastic band method for finding saddle points and minimum energy paths *J. Chem. Phys.* **113** 9901–4
[68] Xu Z, Tian H, Khanaki A, Zheng R, Suja M and Liu J 2017 Large-area growth of multi-layer hexagonal boron nitride on polished cobalt foils by plasma-assisted molecular beam epitaxy *Sci Rep.* **7** 43100
[69] Liu Y, Bhowmick S and Yakobson B I 2011 BN White graphene with 'colorful' edges: the energies and morphology *Nano Lett.* **11** 3113–6
[70] Huber E E and Kirk C T 1966 Work function changes due to the chemisorption of water and oxygen on aluminum *Surf. Sci.* **5** 447–65
[71] Cardwell A B 1949 Photoelectric and thermionic properties of nickel *Phys. Rev.* **76** 125–7
[72] Chauvet C and Laurent C 1993 Weibull statistics in short-term dielectric breakdown of thin polyethylene films *IEEE Trans. Electr. Insul.* **28** 18–29
[73] Cui Z, He Y, Tian H, Khanaki A, Xu L, Shi W and Liu J 2020 Study of direct tunneling and dielectric breakdown in molecular beam epitaxial hexagonal boron nitride monolayers using metal–insulator–metal devices *ACS Appl. Electron. Mater.* **2** 747–55
[74] Bokdam M, Brocks G, Katsnelson M I and Kelly P J 2014 Schottky barriers at hexagonal boron nitride/metal interfaces: a first-principles study *Phys. Rev.* B **90** 085415
[75] Fernandez L, Makarova A A, Laubschat C, Vyalikh D V, Usachov D Y, Ortega J E and Schiller F 2019 Boron nitride monolayer growth on vicinal Ni(1 1 1) surfaces systematically studied with a curved crystal *2D Mater.* **6** 025013
[76] Schwarz M *et al* 2017 Corrugation in the weakly interacting hexagonal-BN/Cu(111) system: structure determination by combining noncontact atomic force microscopy and x-ray standing waves *ACS Nano* **11** 9151–61
[77] Lima L H, Greber T and Muntwiler M 2020 The true corrugation of a h-BN nanomesh layer *2D Mater.* **7** 035006